Taylor & Francis
Taylor & Francis Group

A new 3D 6-node solid finite element based upon the "Space Fibre Rotation" concept

Kamel Meftah[a], Rezak Ayad[b]* and Mabrouk Hecini[c]

[a]*Department of Mechanics, University of Biskra, B.P. 145, R.P., 07000 Biskra, Algeria;* [b]*Laboratoire d'Ingénierie & Sciences des Matériaux (LISM), Université de Reims Champagne-Ardenne, UFR SEN, Moulin de la Housse (15-18), BP 1039, 51687 Reims cedex 2, France;* [c]*Laboratory of Mechanical Engineering, University of Biskra, B.P. 145, R.P., 07000 Biskra, Algeria*

This paper presents the development of a new 6-node solid wedge element with three translational and three rotational degrees of freedom per node. It is based on the model Space Fibre Rotation (SFR). Using the rotation of a material fibre in 3D space, the SFR approach allows to get a more accurate displacement field, which becomes quadratic without changing the number of nodes of the element. It is economical since only two integration points are used. In order to evaluate the usual element stiffness, a small penalty stiffness is introduced so that no zero energy modes appear while preserving the advantage of reduced integration. Several benchmark tests have demonstrated the improved performance of the present element.

Cet article présente le développement d'un élément fini volumique à 6 nœuds avec six degrés de libertés (trois translations et trois rotations) par nœud. Cet élément est basé sur le concept SFR (Space Fiber Rotation). En exploitant la rotation d'une fibre matérielle élémentaire dans l'espace, ce nouveau modèle crée de la valeur en enrichissant la définition du champ des déplacements qui devient quadratique, tout en maintenant le nombre de nœuds de l'élément prismatique linéaire. Pour éliminer les modes à énergie nulle dus à l'intégration réduite (2 points), une matrice de pénalité est introduite. Plusieurs tests d'évaluation ont démontré l'amélioration des performances de cet élément.

Keywords: 3D finite element; wedge element; Space Fibre Rotation; zero-energy modes

Mots-clés: élément fini 3D; élément fini prismatique; fibre spatiale; modes parasites

1. Introduction

In the recent years, large-scale finite element analyses are extensively used in simulating real three-dimensional (3D) engineering applications. The finite element method is an efficient technique of analysing the complex physical phenomena of most structures, because it can reduce dramatically the cost of design process and help engineers to better understand the deformation processes and to control the quality of the products. The application of this method in a large class of problems demands for suitable and robust tools for a flexible and efficient implementation. In the context of the finite element method, in order to meet these

---

*Corresponding author. Email: rezak.ayad@univ-reims.fr

requirements, it is essential to choose and develop appropriate elements to speed up the design processes and reduce the computational costs for these problems. With the advent of more powerful and faster computers, considerable progress has been achieved in developing fast and reliable elements.

The motivation for the development of the 6-node solid wedge element is based on the successful application of corner rotation of two-dimensional (2D) membrane elements. A number of membrane and plate/shell elements using Allman's rotation (Allman, 1984) have been presented in Allman (1984, 1988), Bergan and Felippa (1984), Cook (1986) and MacNeal and Harder (1988). Soon after this, a simple formulation of these 2D elements with rotational degrees of freedom using the hybrid approach has also been studied in Cook (1987) and Yunus (1988). Another recent approach for 2D membrane element is developed by Ayad (1993) which used a virtual plane fibre incorporated at the nodal level, the fibre rotation represented by the fictitious rotation degree of freedom at the 2D element nodes. It also was used by Ghomari, Talbi, Ayad, Kerdal, and Ziane (2006) for improving the accuracy of the standard 4-node element with applications to forming processes of hollow plastics. This method exploits the reduced integration (RI) scheme with the aid of the zero-energy modes control technique so that it can maintain the computational efficiency. The two elements developed by application of this approach are described as: (1) a 3-node triangular element (FRT) does not exhibit hourglass mechanisms and its equal-rotation mechanisms are stabilised by the stabilisation scheme of MacNeal and Harder (1988) and (2) a 4-node quadrilateral element (FRQ) exhibits two unusual types of zero-energy modes (hourglass and equal-rotation mechanisms), in addition to the rigid body movements, but this is very easily suppressed also by the stabilisation schemes of MacNeal and Harder (1988).

The following gives a brief review of the solid elements with rotational degrees of freedom (DOF): much attention has been shifted to the 3D elements; for example, Yunus, Saigal, and Cook (1989) developed a 3D hybrid element with rotational DOF. The equal-rotation mechanisms are left unattended. Other works have followed, such as the one in Yunus, Pawlak, and Cook (1991) and Pawlak, Yunus, and Cook (1991) are solid elements hexahedron and tetrahedron with rotational DOF. The hourglass mechanisms due to the subintegration and the equal-rotation mechanisms were suppressed by generalising the 2D stabilisation schemes of MacNeal (MacNeal, 1989; MacNeal & Harder, 1988). Later, two brick elements equipped with Allman's rotation were developed by Sze, Soh, and Sim (1996). These elements are also plagued by the zero-energy modes that were suppressed by the explicit hybrid stabilisation scheme. It is interesting to note that Sze and Pan (2000) also proposed two hybrid stress tetrahedron elements with Allman's rotational DOF. These elements are improved with the aid of the rotation formulations originating from the work of Allman (1984, 1988) and exhibit four zero-energy modes. The zero-energy modes are controlled by using four skew symmetric stress modes. More recently, Tian, Matsubara, and Yagawa (2006) developed a general purpose tetrahedral element with only corner nodes and using vertex rotational DOF, knowing that, the boundary treatment method removed the zero-energy modes. Other types of the advanced tetrahedron element are developed by Matsubara, Iraha, Tomiyama, Yamashiro, and Yagawa (2004). This element contains also zero-energy modes that are similar to those in tetrahedron element proposed by Pawlak et al. (1991). Further work with 3D case, an 8-node solid element SFR8, developed by Ayad (2003) is based upon the Space Fibre Rotation (SFR) concept. Conceptually, the idea of this method is similar to the 2D membrane element FRQ (Ayad, 1993), knowing that the zero-energy modes corresponding to the RI disappear after the assembly of several elements without introducing stabilising matrices.

In this paper, a 6-node solid wedge element SFR6 based upon the SFR including translations and fictive rotations as nodal DOF is developed for the analysis of 3D elasticity

problems. The intent is to introduce a 6-noded element that is computationally attractive when compared with the 6- and 15-node wedge elements with translations only as DOF. The proposed wedge element SFR6 is developed by exploiting the space rotation of a virtual fibre, this model is called SFR. The classical finite element displacement approximation is enriched by employing additional terms based on the SFR concept. These terms, represented by the fictitious rotational degrees of freedom, would result in the creation of an interesting added value by providing a reliable and accurate solution. This element uses a RI scheme with only two-points (one-point rule in $\xi - \eta$-plane and the second-order quadrature along ζ). Although the RI methods are more advantageous in numerical problems because of their low computational cost, these techniques can lead to instability due to zero-energy modes. In order to eliminate the instability of RI methods, a small penalty stiffness matrix is introduced, using the procedures given by Yunus et al. (1991), Pawlak et al. (1991) and Zienkiewicz (1977).

The organisation of the remainder of the paper is as follows: Section 2 presents basic developments. The variational formulation for solid element is presented herein. The principle of the SFR model and its adaptation to a 6-node wedge element, named SFR6 is also stated. Additionally, examines the RI element which is integrated by the 1×2 rule. Section 3 introduces the penalty stiffness for the zero-energy modes control. In Section 4, 10 examples are presented: firstly, a numerical verification of the patch test is obtained. Nine additional examples, namely, plane bending of a cantilever beam, Cook's membrane problem, clamped circular plate, simply supported 30° skew plate under uniform load, twisted beam, pinched hemisphere, pinched cylindrical shell, clamped beam and a simply supported square plate (shear locking test), illustrate the accuracy increase and efficiency of the presented approach in comparison to the classical displacement-based finite element formulations. Finally, Section 5 presents concluding remarks.

2. Basic formulation

2.1. Variational formulation

We consider a linear elastic body problem in a state of small strains that occupies the domain Ω and its boundary $\partial\Omega$, as shown in Figure 1. The equilibrium equation in the mixed configuration for a body subjected to body forces $\underline{f}^{v}$ is then given by:

$$\text{Div}(\underline{\sigma}) + \underline{f}^{v} = 0 \tag{1}$$

where $\underline{\sigma}$ is the mechanical stress tensor. In order to complete the boundary value problem, the displacement boundary conditions on $\partial\Omega_{u}$ and the traction boundary conditions on $\partial\Omega_{t}$ must be satisfied.
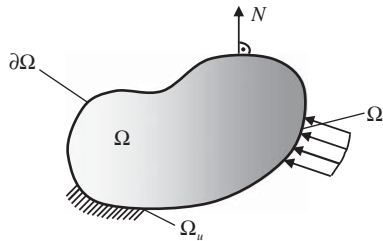

Figure 1. Domain.

$$\begin{cases} u_i &= U_i & \text{on} & \partial\Omega_u \\ \sigma_{ij}n_j &= T_i & \text{on} & \partial\Omega_t \end{cases} \tag{2}$$

where n_i is the ith component of the normal N to the surface of the body in the initial configuration, as shown in Figure 1.

The weak form $\delta\Pi$ of the equilibrium Equation (1) is obtained by introducing the admissible test function $\delta\underline{u}$ verifying $\delta\underline{u} = 0$ on $\partial\Omega_u$ and integrating by parts, using the divergence theorem. The following weak form is obtained:

$$\delta\Pi = \int_{\Omega} \sigma_{ij}\delta\varepsilon_{ij}\mathrm{d}\Omega - \left[\int_{\Omega} f_i^v \delta u_i \mathrm{d}\Omega + \int_{\partial\Omega_t} T_i \delta u_i \mathrm{d}S\right] = \delta W_{\text{int}} - \delta W_{\text{ext}} = 0 \tag{3}$$

where δW_{int} and δW_{ext} are, respectively, the internal and external mechanical virtual works.

The virtual gradient field $\delta\underline{\underline{\varepsilon}}$ is related to $\delta\underline{u}$ by the following expression:

$$\delta\underline{\underline{\varepsilon}} = \frac{1}{2}(\underline{\underline{\text{grad}}}(\delta\underline{u}) + \underline{\underline{\text{grad}}}^{\text{T}}(\delta\underline{u})) \tag{4}$$

From Equation (3), the weak form can be rewritten as follows:

$$\delta\Pi = \int_{\Omega} \{\delta\varepsilon\}^{\text{T}}\{\sigma\}\mathrm{d}\Omega - \left[\int_{\Omega} f_i^v \delta u_i \mathrm{d}\Omega + \int_{\partial\Omega_t} T_i \delta u_i \mathrm{d}S\right] = \delta W_{\text{int}} - \delta W_{\text{ext}} = 0 \tag{5}$$

where $\{\sigma\}$ and $\{\varepsilon\}$ are, respectively, the Cartesian stress and strain vectors given by:

$$\{\sigma\} = \{ \sigma_{xx} \quad \sigma_{yy} \quad \sigma_{zz} \quad \tau_{xy} \quad \tau_{xz} \quad \tau_{yz} \}^{\text{T}} \tag{6a}$$

$$\{\varepsilon\} = \{ \varepsilon_{xx} \quad \varepsilon_{yy} \quad \varepsilon_{zz} \quad \gamma_{xy} \quad \gamma_{xz} \quad \gamma_{yz} \}^{\text{T}} \tag{6b}$$

with $\gamma_{xy} = 2\varepsilon_{xy}$, $\gamma_{xz} = 2\varepsilon_{xz}$ and $\gamma_{yz} = 2\varepsilon_{yz}$.

2.2. Principle of the SFR model

The SFR model is based on the space rotation of a virtual fibre. Figure 2 shows the geometry of 6-node wedge element, in which a virtual space fibre $\underline{iq}$ is incorporated at the nodal level (Ayad, 2003). The fibre rotation, represented by the rotation vector $\underline{\theta}$, will generate an additional displacement vector $f(\underline{\theta}_i, \underline{iq})$ (Equation (7)) that would enrich the classical displacement field $\underline{u}_q$ of point q, used to formulate the standard 6-node solid wedge element.

a. 6-node wedge element SFR6   b. Space fiber iq
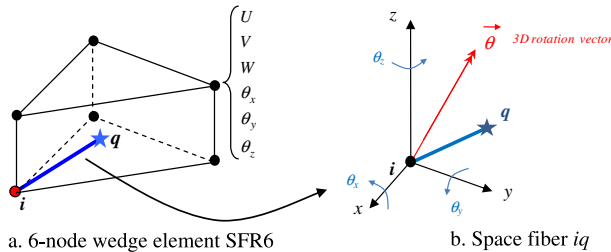
Figure 2.   Geometry and kinematics of a virtual space fibre (SFR approach).

The final displacement field will take the following form:

$$\underbrace{\underline{u}_q}_{\text{Displacement field}} = \underbrace{\sum_i N_i \underline{u}_i}_{\text{Classical approximation of } \underline{u}_q} + \underbrace{f(\underline{\theta}_i, \underline{iq})}_{\text{Additional displacement}} \tag{7}$$

where N_i is the elementary shapes functions and $\underline{u}_i$ is the vector of nodal displacements.

2.3. Approximation of the displacement field for SFR6

The introduction of the rotation vector $\underline{\theta}$ of the virtual space fibre $\underline{iq}$ (Figure 2(b)) leads to an improved expression of the approached displacement field $\overline{\underline{u}}_q$ of q (Ayad, 2003):

$$\underline{u}_q = \sum_{i=1}^{6} N_i \underline{u}_i + f(\underline{\theta}_i, \underline{iq}) \tag{8}$$

where

$$f(\underline{\theta}_i, \underline{iq}) = \sum_{i=1}^{6} N_i(\underline{\theta}_i \wedge \underline{iq}); \quad \{iq\} = \begin{Bmatrix} x - x_i \\ y - y_i \\ z - z_i \end{Bmatrix} \tag{9}$$

and

$$\{u_i\} = \begin{Bmatrix} u_i \\ v_i \\ w_i \end{Bmatrix}; \quad \{\theta_i\} = \begin{Bmatrix} \theta_{xi} \\ \theta_{yi} \\ \theta_{zi} \end{Bmatrix} \tag{10}$$

N_i is the usual 6-node wedge shape functions (Batoz & Dhatt, 1990):

$$\langle N \rangle = \langle\, CA \quad \xi A \quad \eta A \quad CB \quad \xi B \quad \eta B \,\rangle \tag{11}$$

where

$$C = 1 - \xi - \eta; \; A = \frac{1 - \zeta}{2}; \; B = \frac{1 + \zeta}{2} \tag{12}$$

with $\xi \geq 0$, $\eta \geq 0$, $1 - \xi - \eta \geq 0$ and $-1 \leq \zeta \leq 1$.

(x_i, y_i and z_i) are the Cartesian coordinates of node i and (x, y and z) are the Cartesian coordinates of any point q of the element SFR6 given by the following approximations:

$$x = \sum_{i=1,6} N_i x_i \; ; \; y = \sum_{i=1,6} N_i y_i \; ; \; z = \sum_{i=1,6} N_i z_i \tag{13}$$

By performing the vector product $\underline{\theta}_i \wedge \underline{iq}$, we obtain the following approximation of $\underline{u}_q$:

$$\{u_q\} = \begin{Bmatrix} u \\ v \\ w \end{Bmatrix} = \sum_{i=1}^{6} \begin{Bmatrix} N_i u_i + N_i(z - z_i)\theta_{yi} - N_i(y - y_i)\theta_{zi} \\ N_i v_i - N_i(z - z_i)\theta_{xi} + N_i(x - x_i)\theta_{zi} \\ N_i w_i + N_i(y - y_i)\theta_{xi} - N_i(x - x_i)\theta_{yi} \end{Bmatrix} \tag{14}$$

or in a matrix form:

$$\{u_q\} = [N_q]\{u_n\}; \quad [N_q] = \begin{bmatrix} & <N_{ui}> & \\ \cdots & <N_{vi}> & \cdots & i = 1,6 \\ & <N_{wi}> & \end{bmatrix} \tag{15}$$

where

$$\begin{aligned} <N_{ui}> &= \langle N_i & 0 & 0 & 0 & N_i(z - z_i) & -N_i(y - y_i) \rangle \\ <N_{vi}> &= \langle 0 & N_i & 0 & -N_i(z - z_i) & 0 & -N_i(x - x_i) \rangle \\ <N_{wi}> &= \langle 0 & 0 & N_i & N_i(y - y_i) & -N_i(x - x_i) & 0 \rangle \end{aligned} \tag{16}$$

and $\{u_n\}$ is the nodal degrees of freedom vector of SFR6, containing six DOF (three translations and three fictive rotations) per node:

$$<u_n> = <\cdots \quad u_i \quad v_i \quad w_i \quad \theta_{xi} \quad \theta_{yi} \quad \theta_{zi} \quad \cdots \quad i = 1,6 > \tag{17}$$

From the standard displacement-based finite element functions, the strain vector $\{\varepsilon\}$ and the stress vector $\{\sigma\}$ can be expressed as:

$$\{\varepsilon\} = [B]\{u_n\} \tag{18a}$$

$$\{\sigma\} = [H][B]\{u_n\} \tag{18b}$$

where $[B]$ is the strain–displacement matrix, which is:

$$[B] = [L][N_q] \tag{18c}$$

with the 3D strain operator given by:

$$[L] = \begin{bmatrix} \frac{\partial}{\partial x} & 0 & 0 & \frac{\partial}{\partial y} & \frac{\partial}{\partial z} & 0 \\ 0 & \frac{\partial}{\partial y} & 0 & \frac{\partial}{\partial x} & 0 & \frac{\partial}{\partial z} \\ 0 & 0 & \frac{\partial}{\partial z} & 0 & \frac{\partial}{\partial x} & \frac{\partial}{\partial y} \end{bmatrix}^{\mathrm{T}} \tag{18d}$$

Therefore, the strain-displacement matrix can be written in the following form:

$$[B] = \begin{bmatrix} \langle N_{u,x} \rangle \\ \langle N_{v,y} \rangle \\ \langle N_{w,z} \rangle \\ \langle N_{u,y} \rangle + \langle N_{v,x} \rangle \\ \langle N_{u,z} \rangle + \langle N_{w,x} \rangle \\ \langle N_{v,z} \rangle + \langle N_{w,y} \rangle \end{bmatrix} \text{(Dim. } 6 \times 36) \tag{19}$$

The derivatives of the shape functions with respect to the global axes (x, y and z) are obtained in the standard way as:

$$
\begin{aligned}
\langle N_{\alpha,x}\rangle &= j_{11}\langle N_{\alpha,\xi}\rangle + j_{12}\langle N_{\alpha,\eta}\rangle + j_{13}\langle N_{\alpha,\zeta}\rangle \\
\langle N_{\alpha,y}\rangle &= j_{21}\langle N_{\alpha,\xi}\rangle + j_{22}\langle N_{\alpha,\eta}\rangle + j_{23}\langle N_{\alpha,\zeta}\rangle; \quad \alpha \equiv u, v, w \\
\langle N_{\alpha,z}\rangle &= j_{31}\langle N_{\alpha,\xi}\rangle + j_{32}\langle N_{\alpha,\eta}\rangle + j_{33}\langle N_{\alpha,\zeta}\rangle
\end{aligned}
\tag{20}
$$

where j_{lk} are the inverse Jacobian matrix components.

The Jacobian matrix is defined as follows:

$$
[J] = \begin{bmatrix}
x_{,\xi} & y_{,\xi} & z_{,\xi} \\
x_{,\eta} & y_{,\eta} & z_{,\eta} \\
x_{,\zeta} & y_{,\zeta} & z_{,\zeta}
\end{bmatrix}
\tag{21}
$$

where it is calculated from the Cartesian coordinates of point q (Equation (13)).

The minimisation of the total potential energy with respect to the nodal displacements $\{u_n\}$ results in:

$$
\begin{aligned}
\frac{\delta \Pi^e}{\{\delta u_n\}} &= \left[\int_{V^e}[B]^T[H][B]\mathrm{d}V^e\right]\{u_n\} - \left\{\int_{V^e}[N_1]^T\{f_v\}\mathrm{d}V^e + \int_{S^e}[N_1]^T\{T\}\mathrm{d}S^e\right\} \\
&= [K^e]\{u_n\} - \{F^e\} = 0
\end{aligned}
\tag{22}
$$

where $[N_1]$ is a (3×36)-sized matrix relating the mechanical displacement vector of q to the nodal degrees of freedom vector $\{u_n\}$, $\{F^e\}$ is the equivalent nodal force vector and $[K^e]$ is the stiffness matrix written as follows:

$$
[K^e] = \int_{V^e}[B]^T[H][B]\mathrm{d}V^e\,(\text{Dim. } 36 \times 36)
\tag{23}
$$

The elasticity matrix for a 3D problem can be written, for a homogeneous and isotropic material, as:

$$
[H] = \begin{bmatrix}
2G + \lambda & \lambda & \lambda & 0 & 0 & 0 \\
\lambda & 2G + \lambda & \lambda & 0 & 0 & 0 \\
\lambda & \lambda & 2G + \lambda & 0 & 0 & 0 \\
0 & 0 & 0 & G & 0 & 0 \\
0 & 0 & 0 & 0 & G & 0 \\
0 & 0 & 0 & 0 & 0 & G
\end{bmatrix}
\tag{24a}
$$

The Lamé coefficients are expressed in terms of Young's modulus, E, and Poisson's ratio, v, by:

$$
\lambda = \frac{Ev}{(1+v)(1-2v)} \quad \text{and} \quad G = \frac{E}{2(1+v)}
\tag{24b}
$$

2.4. Numerical integration implementation

The integration domain for a 6-node wedge element (SFR6) consists of a prism with triangular lower and upper surface (Figure 3). The approximation of the part corresponding to the rotation of space fibre is quadratic in terms of ξ, η and ζ.

This 6-node wedge element is usually integrated with a nine-points scheme (Dhondt, 2004). We found that the RI scheme with two points makes the element SFR6 particularly effective, without affecting the numerical results.

3. Zero-energy mode control

The stiffness matrix for the 6-node wedge element has 18 unknown fictive rotational degrees of freedom at the nodes. An examination of the properties of the stiffness matrix indicates that it has zero-energy modes in addition to the six rigid body modes. These zero-energy modes can be controlled through the introduction of penalty stiffnesses. The element stiffness matrix integrated exactly using a nine-point rule (Dhondt, 2004) has five zero-energy modes and when reduced integrated using a two-point rule (Dhondt, 2004) has 18 zero-energy modes. The stabilisation technique used in SFR6 is designed to suppress the zero-energy modes, this technique is taken from Yunus et al. (1991) and Pawlak et al. (1991) based on penalty stiffnesses in each of the faces.

The five equal rotations zero-energy modes (Figure 4) and the three hourglass modes (Figure 5) can easily be controlled by using a small penalty stiffness similar to that proposed by MacNeal and Harder (1988) for each of the five faces of the wedge. The remaining 10 zero-energy modes are suppressed by associating a fictitious rotational stiffness (Batoz & Dhatt, 1992; Zienkiewicz, 1977) to the in-plane rotational degree of freedom of all the faces of the wedge element, but there is no physical reasoning for the use of such fictitious stiffness.
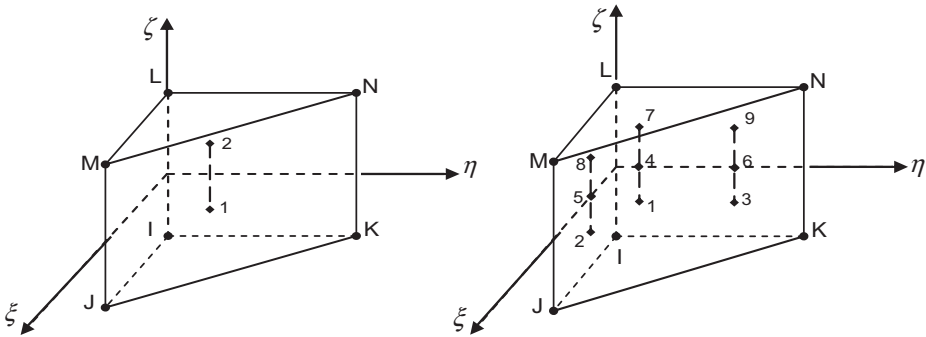

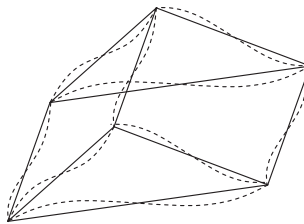Figure 3. Two and nine integration point locations for wedges.

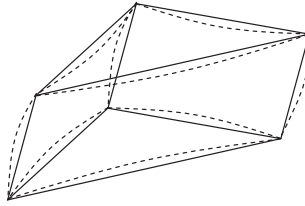Figure 4. Equal rotation zero-energy mode for a single wedge element.

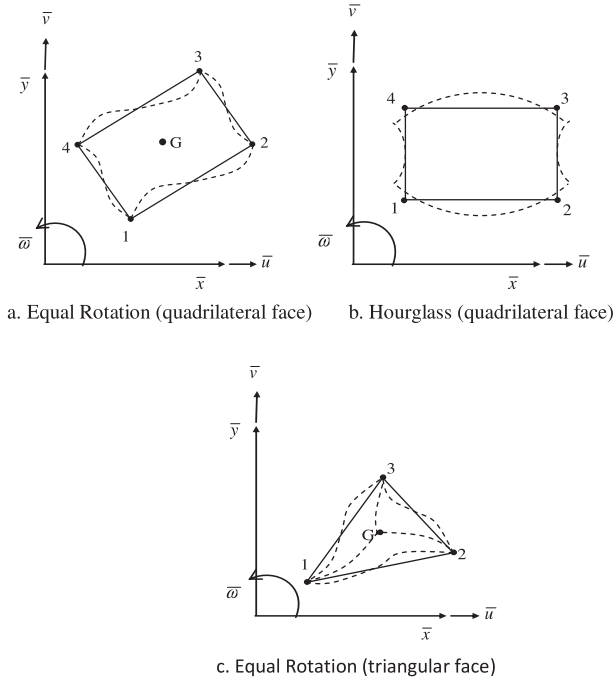Figure 5.   Hourglass mode for single wedge element.

a. Equal Rotation (quadrilateral face)   b. Hourglass (quadrilateral face)

c. Equal Rotation (triangular face)

Figure 6.   Zero-energy modes in single face of wedge elements.

Three penalty stiffnesses are developed per face, one to control the face's equal rotation zero-energy mode, second to control the face's hourglass mode only for the quadrilateral face and another to control the face's fictitious rotational. These face by face penalty stiffnesses define a local zero-energy mode control scheme.

To introduce penalty stiffnesses in order to control the zero-energy modes, consider any face of a wedge and assume that the face lies in a local $\bar{x} - \bar{y}$ plane (see Figure 6).

Although the face plane of a wedge may be warped, requiring 3D surface definition, for the purpose of introducing the penalty stiffnesses, a flat projected plan through the centre of the face is defined and Figure 6 represents such a projected face (Pawlak et al., 1991; Yunus et al., 1991).

3.1.   *Equal rotation control*

The zero-energy displacement modes have equal rotations and zero displacements at all nodes, as shown in Figure 4. To eliminate these modes, it is only necessary to add a rank

one matrix to all five faces (one of such mode is shown in Figure 6(a) and (c)) for wedge element stiffness matrix that has stiffness associated with these modes.

The relative rotation $\bar{\theta}_r$ is defined to be the difference between the average of the out-of-plane nodal rotation degrees of freedom and the average rotation $\bar{\theta}_0$ computed directly from the element shape functions as:

$$\bar{\theta}_r = \frac{1}{n}\sum_{i=1}^{n}(\bar{\omega}_i - \bar{\theta}_0) \tag{25}$$

where n is the number of nodes (4) for the quadrilateral face and (3) for the triangular face and $\bar{\omega}_i$ is the out-of-plane rotation at any node i.

From the elasticity definition of rotation, the average rotation $\bar{\theta}_0$ is evaluated as the rotation of the 4-node quadrilateral and 3-node triangular element computed at the element centre and is only function of the translational degrees of freedom:

$$\bar{\theta}_0 = \frac{1}{2}\left(\frac{\partial \bar{v}}{\partial \bar{x}} - \frac{\partial \bar{u}}{\partial \bar{y}}\right) \tag{26}$$

$\bar{u}$ and $\bar{v}$ are the in-plane translations in the face coordinate system and $\bar{x}$, $\bar{y}$ are the face system coordinates.

The relative rotation $\bar{\theta}_r$ can be expressed in terms of face system nodal DOF $\bar{u}_i$, $\bar{v}_i$ and $\bar{\omega}_i$:

$$\bar{\theta}_r = \langle Q \rangle \{\bar{\delta}\} \tag{27}$$

where $\{\bar{\delta}\} = \{\bar{u}_i \quad \bar{v}_i \quad \bar{\omega}_i\}^{\mathrm{T}}$ are the face system nodal unknowns and $\langle Q \rangle$ is the relative rotation in terms of face system unknowns ($\langle Q \rangle = \langle Q_q \rangle$ for quadrilateral face or $\langle Q \rangle = \langle Q_t \rangle$ for triangular face).

The energy penalty (P_1) is:

$$P_1 = (\alpha_1 VG)\langle\bar{\delta}\rangle\{Q\}\langle Q\rangle\{\bar{\delta}\} \tag{28}$$

where α_1 is a scaling small factor (10^{-6} in MacNeal and Harder (1988), Yunus et al. (1991) and Pawlak et al. (1991)), G is the shear modulus and V is the volume of the wedge element.

The matrix $[T]$ transforms the global DOF into the local face DOF:

$$\{\bar{\delta}_i\} = [T]\{\delta_i\} \tag{29}$$

$[T]$ consists of direction cosines between the global and local face coordinate systems. At each node, i, the relation between the local face and global DOF is expressed as:

$$\begin{Bmatrix} \bar{u}_i \\ \bar{v}_i \\ \bar{\omega}_i \end{Bmatrix} = \begin{bmatrix} l_{11} & l_{12} & l_{13} & 0 & 0 & 0 \\ l_{21} & l_{22} & l_{23} & 0 & 0 & 0 \\ 0 & 0 & 0 & l_{31} & l_{32} & l_{33} \end{bmatrix} \begin{Bmatrix} u_i \\ v_i \\ w_i \\ \theta_{xi} \\ \theta_{yi} \\ \theta_{zi} \end{Bmatrix} \tag{30}$$

where l_{ij} is the direction cosine between the local face axis and the global axis. $u_i, v_i, w_i, \cdots, \theta_{zi}$ are the global unknown at node i.

Then the relationship for the quadrilateral face unknowns $\{\bar{\delta}\}$ with the related global unknowns $\{\delta\}$ is:

$$\{\bar{\delta}\} = \begin{bmatrix} [T] & & & \\ & [T] & & \\ & & [T] & \\ & & & [T] \end{bmatrix} \{\delta\} = [\tau_q]\{\delta\} \tag{31a}$$

and for the triangular face:

$$\{\bar{\delta}\} = \begin{bmatrix} [T] & & \\ & [T] & \\ & & [T] \end{bmatrix} \{\delta\} = [\tau_t]\{\delta\} \tag{31b}$$

Equations (28) and (31) are now combined to obtain:

$$\begin{aligned} P_1 &= (\alpha_1 VG)\langle\delta\rangle[\tau]^{\mathrm{T}}\{Q\}\langle Q\rangle[\tau]\{\delta\} \\ &= \langle\delta\rangle[K_r]\{\delta\} \end{aligned} \tag{32}$$

where

$$[K_r] = (\alpha_1 VG)[\tau]^{\mathrm{T}}\{Q\}\langle Q\rangle[\tau] \tag{33}$$

and $[\tau] = [\tau_q]$ for quadrilateral face and $[\tau] = [\tau_t]$ for triangular face.

The penalty stiffness $[K_r]$ is added to the appropriate terms of element stiffness matrix $[K^e]$ and the resulting stiffness matrix is free from zero-energy equal rotation. It should be clear that if the new 6-node wedge element is integrated using a nine-point rule then no other zero-energy modes will appear.

3.2. Hourglass control

The application of RI (two points) may produce a mesh distortion which is related to zero energy or so-called hourglass modes (Flanagan & Belytschko, 1981). The hourglassing modes are usually identified with a right parallelepiped and are represented by alternating rotations plus additional corner translations (one of these zero-energy modes is shown in Figure 6(b)). The method was developed previously by Yunus et al. (1991) and is applicable to all the quadrilateral faces of the wedge element. Hourglass control is included to remove the three zero-energy modes from an element. For certain finite element meshes, these modes may not exist after the element stiffness matrices have been added and boundary conditions applied.

The mode configuration for the quadrilateral face of the wedge element is written as:

$$\bar{\theta}_h = (\bar{\omega}_1 - \bar{\omega}_2 + \bar{\omega}_3 - \bar{\omega}_4) \tag{34a}$$

$$\bar{\theta}_{h} = \langle\, 0 \quad 0 \quad 1 \quad 0 \quad 0 \quad -1 \quad 0 \quad 0 \quad 1 \quad 0 \quad 0 \quad -1 \,\rangle \left\{ \begin{array}{c} \bar{u}_1 \\ \bar{v}_1 \\ \bar{\omega}_1 \\ \vdots \\ \bar{\omega}_4 \end{array} \right\} \tag{34b}$$

Symbolically,

$$\bar{\theta}_{h} = \langle H\rangle\{\bar{\delta}\} \tag{35}$$

The penalty function associated with each quadrilateral face is:

$$P_2 = (\alpha_2 VG)\langle\bar{\delta}\rangle\{H\}\langle H\rangle\{\bar{\delta}\} \tag{36}$$

where α_2 is a scaling small factor (10^{-3}) in MacNeal and Harder (1988) and Yunus et al. (1991).

Now by using the transformation relation between the face and global element systems (Equation 31(a)), the penalty function is rewritten as:

$$P_2 = (\alpha_2 VG)\langle\delta\rangle[\tau_q]^{\mathrm{T}}\{H\}\langle H\rangle[\tau_q]\{\delta\} = \langle\delta\rangle[K_h]\{\delta\} \tag{37}$$

where

$$[K_h] = (\alpha_2 VG)[\tau_q]^{\mathrm{T}}\{H\}\langle H\rangle[\tau_q] \tag{38}$$

The penalty stiffness matrix $[K_h]$ for the hourglass modes for each of the faces is then added to the appropriate location of the global stiffness matrix $[K^e]$, so that this new augmented stiffness matrix does not have any hourglassing modes.

3.3. The fictitious rotational stiffness

The use of fictitious rotational stiffness has been proposed by Zienkiewicz (1977) and used by Batoz and Dhatt (1992) to avoid the problem of singularity in element stiffness matrix. The fictitious rotational stiffness available to control the remaining 10 (two for face) zero-energy modes is calculated in the local coordinate system for all faces. This matrix of rank equal two is associated with local rotation variables $\bar{\omega}_i$. The fictitious rotational stiffness is evaluated of the 4-node quadrilateral and 3-node triangular Laplacian elements (Batoz & Dhatt, 1990). The penalty function associated with each face lying in a local $\bar{x}, \bar{y}$ plane is:

$$P_3 = \alpha_3 C \int_A (\bar{\omega}^*_{,x} \cdot \bar{\omega}_{,x} + \bar{\omega}^*_{,y} \cdot \bar{\omega}_{,y})\,\mathrm{d}A = \langle\bar{\omega}^*_n\rangle[K_{\bar{\omega}}]\{\bar{\omega}_n\} \tag{39}$$

where $[K_{\bar{\omega}}]$ is fictitious rotational stiffness associating to the in-plane rotational degree of freedom $\bar{\omega}_i$ of the face coordinates.

$\{\bar{\omega}_n\} = \{\bar{\omega}_1 \quad \bar{\omega}_2 \quad \bar{\omega}_3\}^{\mathrm{T}}$ for triangular face or $\{\bar{\omega}_n\} = \{\bar{\omega}_1 \quad \bar{\omega}_2 \quad \bar{\omega}_3 \quad \bar{\omega}_4\}^{\mathrm{T}}$ for quadrilateral face.

$\alpha_3 = \frac{2V}{L^2_{\max}}$ is a scaling small factor inspired of Ayad (1993).

$C = \frac{EV}{12}$ is a value inspired of Batoz and Dhatt (1992).

$L_{\max}$ is the maximum length of the edges of the wedge element.

The matrix $[T_3]$ transforms the global fictive rotational degrees of freedom into the local face fictive rotational degrees of freedom with each node i is:

$$\{\bar{\omega}_i\} = [T_3]\{\theta_i\} \tag{40}$$

$$\{\bar{\omega}_i\} = \begin{bmatrix} l_{31} & l_{32} & l_{33} \end{bmatrix} \begin{Bmatrix} \theta_{xi} \\ \theta_{yi} \\ \theta_{zi} \end{Bmatrix} \tag{41}$$

where l_{ij} is the direction cosine between the local face axis $\bar{z}$ and the global axis.

The relationship between the local face unknown fictive rotational DOF $\{\bar{\omega}\}$ and the global fictive rotational DOF $\{\theta\}$ is:

$$\{\bar{\omega}\} = [\tau_3]\{\theta\} \tag{42}$$

where $[\tau_3] = \begin{bmatrix} [T_3] & & \\ & [T_3] & \\ & & [T_3] \end{bmatrix}$ for 3-node triangular face.

or $[\tau_3] = \begin{bmatrix} [T_3] & & & \\ & [T_3] & & \\ & & [T_3] & \\ & & & [T_3] \end{bmatrix}$ for 4-node quadrilateral face.

So, the fictitious rotational stiffness associated in unknowns fictive rotational DOF is rewritten as:

$$[K_f] = [\tau_3]^{\mathrm{T}}[K_{\bar{\omega}}][\tau_3] \tag{43}$$

The penalty stiffnesses $[K_f]$ for the fictitious rotational for each of the quadrilateral face and triangular face are then added to the appropriate location of the global stiffness matrix $[K^e]$ and this new augmented stiffness matrix will not have zero-energy modes.

We conclude the section that the zero-energy modes in SFR6 using the RI, which are the 18 zero-energy modes, are identified to be the rigid body modes. They can be suppressed by including small penalty stiffness to augment the usual element stiffness. To address the issue of selecting a penalty parameter value for α_1, α_2 and α_3, a set numerical experiment is performed.

4. Numerical examples

Ten various benchmark problems, selected from the literature (Batoz & Dhatt, 1990; Cook, Malkus, & Plesha, 1989; Lindberg, Olson, & Cowper, 1969; MacNeal & Harder, 1985; Taylor, Simo, Zienkiewicz, & Chan, 1986; etc.), which are listed in Table 1, have been used to evaluate the performance of the proposed solid element. Firstly, some variants of the Patch test are satisfied. After that, several linear elastic tests are performed. We compare the convergence of the results solved by other element models. Table 2 gives the 2D and 3D elements used here as reference, as well as the abbreviations used in the text. RI scheme with two points is used to evaluate all the numerical examples. All the computations were carried out in code REFLEX (Batoz & Dhatt, 1990), a Fortran 90 code developed by the first author of this work.

Table 1. List of eight benchmark problems.

No.	Benchmark problems, Figure number	Results
1	Patch test, Figure 7	Tables 3 and 4
2	Plane bending of a cantilever beam, Figure 8	Table 5
3	Cook's membrane problem, Figure 9	Table 6
4	Clamped circular plate, Figure 10	Table 8; Figure 11
5	Simply supported 30° skew plate, Figure 12	Table 9; Figure 13
6	Twisted beam, Figure 14	Table 11
7	Pinched hemisphere, Figure 15	Table 12; Figure 16
8	Pinched cylindrical shell, Figure 17	Table 13; Figure 18
9	Clamped beam, Figure 19	Table 14
10	Simply supported square plate, Figure 20	Table 15; Figure 21

Table 2. List of element models for comparison.

Symbols	Explanation	Integration points	Refs.
2D elements			
T3 (CST)	3-node linear triangular element	1 (EI)	–
T6 (LST)	6-node quadratic triangular element	3 (EI)	–
FRT	3-node triangular element based upon the "Plane Fibre Rotation" concept	1 (RI)	Ayad (1993)
3D elements			
W6	6-node linear wedge element	2 (EI)	–
W15	15-node quadratic wedge element	9 (EI)	–
SHB6	6-node solid-shell finite element based on the assumed strain method	5	Trinh et al. (2011)
SFR6	6-node wedge element based upon the "Space Fibre Rotation" concept	2 (RI)	This paper

Note: RI = reduced integration and EI = exact integration.

The mechanical boundary conditions used for SFR6 element are exactly the same as that used for shell finite elements. For example, for clamped boundary conditions, we restrained the displacements and rotational degrees of freedom.

4.1. Patch test

The Patch test A and C for solids introduced by Taylor et al. (1986) is here explored. The purpose of this test is to verify the correctness of the computer implementation of the element. The tests are performed on a distorted hexahedral patch composed of two wedge elements shown in Figure 7. Initial coordinates (x, y and z) at the eight nodes of the patch are given in Table 3. The material is linear, elastic and isotropic with properties of Young's modulus $E = 1000 \, \text{N/mm}^2$ and the Poisson coefficient v is .3.

The Case A is materialised by a homogeneous state of stress with:

$$\sigma_x = 2\text{N/mm}^2, \ \sigma_y = \sigma_z = 0 \tag{44}$$

The analytical solution is obtained by substituting the strain calculated using Hooke's Law, we have the constitutive relations:
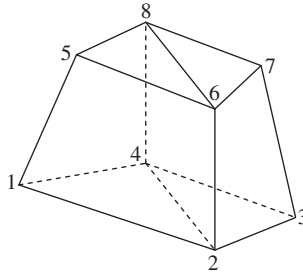
Figure 7. Patch test: distorted hexahedral patch composed of two wedge elements.

Table 3. Patch test: nodal point coordinates (*x*, *y* and *z*), steady-state displacements, forces and moments at eight nodes.

Node no.	Coordinates			Displacements			Forces			Moments		
	x	y	z	u	v	w	F_x	$F_y = F_z$	M_x	M_y	M_z
1	1.5	1.0	.0	.003	−.0006	.0	−1.3749	.0	.0	−.9131	1.2083
2	4.5	1.5	.0	.009	−.0009	.0	2.3125	.0	.0	1.5260	−1.2847
3	4.0	3.5	.0	.008	−.0021	.0	1.4374	.0	.0	.9826	1.2786
4	1.5	3.0	.0	.003	−.0018	.0	−2.5833	.0	.0	−1.9027	−1.3576
5	2.0	1.5	2.0	.004	−.0009	−.0012	−1.0000	.0	.0	.6788	.4036
6	4.25	1.75	2.0	.0085	−.00105	−.0012	2.0416	.0	.0	−1.2256	−.6788
7	3.75	3.0	2.5	.0075	−.0018	−.0015	1.2708	.0	.0	−1.2829	.5980
8	2.0	2.5	2.5	.004	−.0015	−.0015	−2.1041	.0	.0	2.1371	−.1675

$$\varepsilon_x = \frac{1}{E}(\sigma_x - v(\sigma_y + \sigma_z)) = \frac{\sigma_x}{E} = .002 \tag{45a}$$

$$\varepsilon_y = \frac{1}{E}(\sigma_y - v\,(\sigma_x + \sigma_z)) = -v\frac{\sigma_x}{E} = -.0006 \tag{45b}$$

$$\varepsilon_z = \frac{1}{E}(\sigma_z - v(\sigma_x + \sigma_y)) = -v\,\frac{\sigma_x}{E} = -.0006 \tag{45c}$$

Into the strain-displacement relations:

$$u = \varepsilon_x x, \ \ v = \varepsilon_y y, \ \ w = \varepsilon_z z \tag{46}$$

The resulting values for the displacements (*u*, *v* and *w*) at all eight nodes are given in Table 3. Next, these displacements field is imposing at all nodes for the finite element backward calculation with the hexahedral patch (Mahnken, Caylak, & Laschet, 2008). For Case A, whose results are presented in Table 4, the analytical values are reproduced exactly, a condition established in MacNeal and Harder (1985) and known to ensure convergence of results as mesh is refined (Areias, Cesar, Antonio, & Fernandes, 2003). As expected, the stresses state with: $\sigma_x = 2\text{N/mm}^2$, $\sigma_y = \sigma_z = 0$ are obtained in two integration points.

Table 4. Homogeneous stress obtained at all integration points with SFR6.

	Stress component		
	σ_x	σ_y	σ_z
Case A			
Max. value	2	≈ 0	≈ 0
Min. value	2	≈ 0	≈ 0
Theory	2	0	0
Case C			
Max. value	1.99	≈ 0	≈ 0
Min. value	1.93	≈ 0	≈ 0
Theory	2	0	0

Finally, Case C is tested using the forces and moments obtained from the finite element calculation presented in Table 3. The nodes 1, 2, 3 and 4 are fixed in the *w*-direction, nodes 1 and 2 in *u*-direction and node 2 in *v*-direction. The results are presented in Table 4 which verifies the patch test.

(a) Regular meshes

(b) Distorted meshes
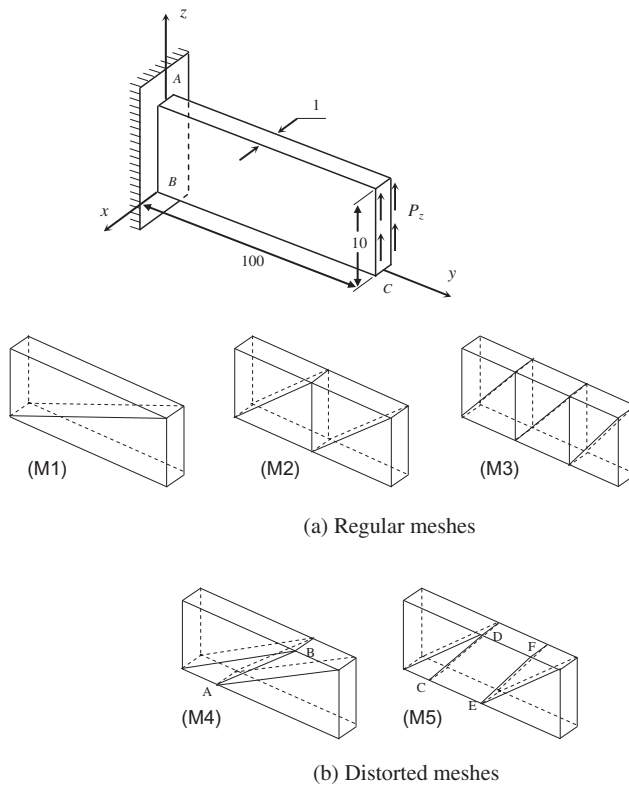
A(1,25,0) ; B(1,75,10) ; C(1,16.7,0) ; D(1,50,10) ; E(1,50,0) ; F(1,83.3,10)

Figure 8. Plane bending of a cantilever beam and 3D meshing.

4.2. Plane bending of a cantilever beam

A cantilever beam subjected to a uniform vertical load at the free end is examined as shown in Figure 8 and is a famous benchmark for testing the sensitivity to mesh distortion. The five mesh shapes are adopted and are shown in Figure 8. The material properties are: Young's modulus $E = 10^7$ and the Poisson's ratio $v = .3$. We investigate the maximum displacement of the beam, which is modelled with two, four and six elements and compare the results with those obtained using the engineering beam theory: $w_C^{ref} = 4.03$. This problem was dealt with by Batoz and Dhatt (1990) in order to test the performances of 2D membrane elements (CST, LST …). Ayad (1993) made a similar study to test the reliability of these new 2D elements FRQ and FRT based on the concept (Plane Fibre Rotation). For comparison reasons, reduced and exact integration (EI) techniques have also been implemented.

The results obtained for different meshes are presented in Table 5. The present results correspond to the SFR6 element with exact and RI rules. It is found that using RI rule tends to overestimate displacements. Also, the SFR6 and FRT elements do not present significant difference in the numerical solutions. For regular mesh, the new element presented in this paper using SFR possesses the best performance compared by classical 6-node wedge element. Besides, the SFR6 solution is shown to be equivalent to that of the 15-node wedge element for the same total degrees of freedom number. For the distorted meshes, it can be seen again that the model is insensitive to mesh distortion than 6-node wedge element with translations only as DOF.

4.3. Cook's membrane problem

This example, in which a skew cantilever was proposed by Cook et al. (1989), the geometry and the finite element discretisation are shown in Figure 9, shear distributed load at the free edge. This test also displays the effects of mesh distortion and showing the shear-dominated

Table 5. The resultants of plane bending of a cantilever beam.

	3D elements				2D elements			
	SFR6		W6	W15	T3 (CST)	T6 (LST)	FRT	
Meshes	EI: 3×3	RI: 2×1	EI: 2×1	EI: 3×3	EI: 1	EI: 3	EI: 3	RI: 1
M1	.24 (48)	2.32 (48)	.05 (24)	3.00 (66)	.05 (8)	3.00 (18)	.24 (12)	2.32 (12)
M2	.89 (72)	2.92 (72)	.14 (36)	3.70 (108)	.14 (12)	3.70 (30)	.89 (18)	2.92 (18)
M3	1.54 (96)	3.07 (96)	.26 (48)	3.84 (150)	.26 (16)	3.84 (42)	1.54 (24)	3.07 (24)
M4	.44 (72)	1.99 (72)	.06 (36)	3.02 (108)	.06 (12)	3.02 (30)	.44 (18)	1.99 (18)
M5	.65 (96)	2.02 (96)	.10 (48)	3.09 (150)	.10 (16)	3.09 (42)	.65 (24)	2.02 (24)

Analytical (Engineering Beam Theory): $w_C^{ref} = 4.03$

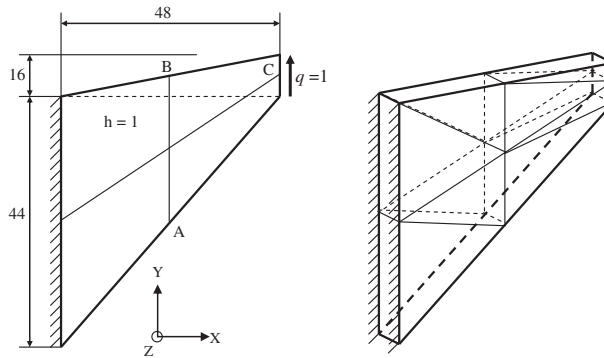Note: Number of degrees of freedom denoted in parenthesis.

Figure 9. Cook's Problem ($E = 1.0$, $v = 1/3$): Left, geometry. Right, finite element mesh consisting of $(2 \times 2 \times 1) \times 2$ wedge elements.

behaviour. The results of vertical deflection at point C, the maximum principle stress at point A and the minimum principle stress at point B are listed in Table 6. In this problem, the present element is also compared to the 2D elements and 3D elements. The presented element exhibits the best convergence of displacements and stresses compared to the corresponding non-rotational element W6. The performance of the element is comparable with that of the W15 element. Judging from three significant meshes, FRT and the present element yield identical results.

Table 6. Results of Cook's problem.

Elements		Mesh: (elem. along the length × elem. along the width × thick. Elem.) × 2		
		$2 \times 2 \times 1$	$4 \times 4 \times 1$	$8 \times 8 \times 1$
Deflection at point C: V_C (reference solution: 23.96 Yuqiu &Yin, 1994)				
2D elements	FRT	21.20	22.88	23.57
	CST	11.99	18.28	22.02
	LST	23.07	23.75	23.87
3D elements	W6	11.99	18.28	22.02
	W15	23.07	23.75	23.87
	SFR6	21.20	22.88	23.57
Max. principle stress at point A: $\sigma_{A\max}$ (reference solution: .2362 Yuqiu &Yin, 1994)				
2D elements	FRT	.175	.213	.233
	CST	.076	.149	.199
	LST	.261	.260	.242
3D elements	W6	.076	.149	.199
	W15	.261	.260	.242
	SFR6	.175	.213	.233
Min. principle stress at point B: $\sigma_{B\min}$ (reference solution: −.2023 Yuqiu &Yin, 1994)				
2D elements	FRT	−.308	−.176	−.200
	CST	−.059	−.099	−.156
	LST	−.216	−.205	−.202
3D elements	W6	−.059	−.099	−.156
	W15	−.216	−.205	−.202
	SFR6	−.308	−.176	−.200

4.4. *Clamped circular plate*

Figure 10 shows a quadrant of a clamped circular plate under uniform loading modelled by $N=8$, 18, 76 and 128 elements. For W15, only one element is used in the through-thickness direction, while for W6 and SFR6 two elements are considered. This classical benchmark problem is used to demonstrate that 3D solid elements are free from shear locking when irregular shaped elements are used. The geometric and material data are specified in Table 7. The reference solution is quoted by Timoshenko and Woinowsky–Krieger (1961). Some results of the given problem solution are given in Table 8 and are compared with the results by W6 and W15 elements. The performance of our element is quite satisfying and demonstrates a rather quick convergence to the exact values compared by the W6 element. For the ratio $R/h=50$ and 5, the numerical results are always more accurate than the W6 element in all mesh configurations which get closer to that of W15 element. For the ratio $R/h=2$, the SFR6 element is more accurate than the 15-node wedge element W15. The normalised central
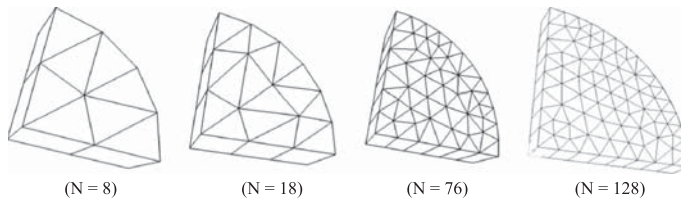

| (N = 8) | (N = 18) | (N = 76) | (N = 128) |

Figure 10.   Circular plate meshes.

Table 7.   Geometric and material data.

Radius	$R=5$
Thickness	$h=.1$, 1.0 and 2.5 ($R/h=50$, 5 and 2)
Young's modulus and Poisson's ratio	$E=10.92$; $v=.3$
Load	$q=1.0$

Table 8.   Central deflections for clamped circular plate.

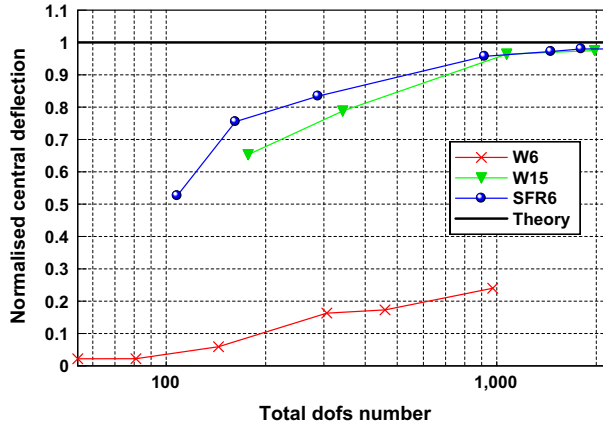|			N		
Elements	8	18	76	128	Theory
$R/h=50$					
W6	215.24	578.29	1591.3	2337.2	9783.51
W15	6395.4	7717.2	9430.5	9541.8	
SFR6	7385.3	8159.2	9368.2	9504.6	
$R/h=5$					
W6	7.001	8.701	9.951	10.11	11.55
W15	10.45	10.55	10.99	11.26	
SFR6	9.175	10.03	11.04	11.32	
$R/h=2$					
W6	1.126	1.153	1.171	1.180	1.339
W15	1.177	1.186	1.204	1.211	
SFR6	1.237	1.237	1.333	1.337	

Figure 11.   Normalised central deflection for clamped circular plate ($R/h = 50$).

deflection for plate thickness $h = .1$ ($R/h = 50$) with respect to the total number of degrees of freedom in a log scale is shown in Figure 11. From this figure, it can be found that the present element can converge to the exact solution more quickly.

4.5.   *Skew plate under uniform load*

We consider the plate bending problem shown in Figure 12, this model was first studied by Morley (1963). The square plate of dimension $L \times L$, with uniform thickness h, material properties $E = 10.92$, $v = .3$, is a simply supported 30° skew plate subject to uniform pressure. Five meshes are used consisting of $N = 4$, 8, 16, 24 and 32 elements on each side. For that case, only one W15 element in the thickness direction is used, while two for W6 and SFR6. The typical geometry of the skew plate analysed are shown in Figure 12, where an example of a 4×4 ($N = 4$) mesh which consists of $(4 \times 4 \times 1) \times 2$ elements is also shown. The normalised values of the deflection at the central point are given in Table 9 for different plate thickness ($h = .1$ and 1.0). The results obtained for the SFR6 element are significantly better than the standard 6-node wedge element. We also compare the results obtained with the SFR6 element and
15-node wedge element. Figure 13 presents the convergence of the normalised central deflections under the total number of degrees of freedom in a log scale. It is found that the SFR6 element used is slightly more accurate than the W15 element for thin plate ($L/h = 1000$). In
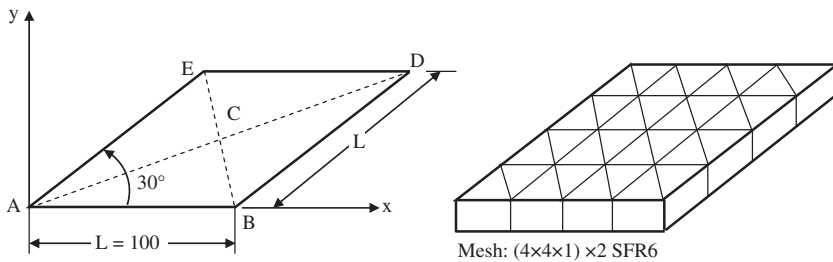

Figure 12.   The 30° skew plate: subjected to uniform load ($q = 1.0$), and is simply supported on all four edges (boundary condition: $w = 0$).

Table 9. Normalised central deflections for 30° skew plate.

Elements	N					Reference
	4	8	16	24	32	$[\overline{w}_c = w_c 10^3 D/qL^4]$
L/h = 1000						
W6	.001	.005	.022	.046	.145	Kirchhoff plate theory Morley (1963)
W15	.632	.691	.794	.865	.912	.408
SFR6	.752	.870	.922	.943	.972	
L/h = 100						
W6	.130	.306	.553	.691	.732	3D solution (Babuska & Scapolla, 1989)
W15	.781	.946	1.010	1.012	1.001	.4235
SFR6	.755	.872	.929	.948	.985	
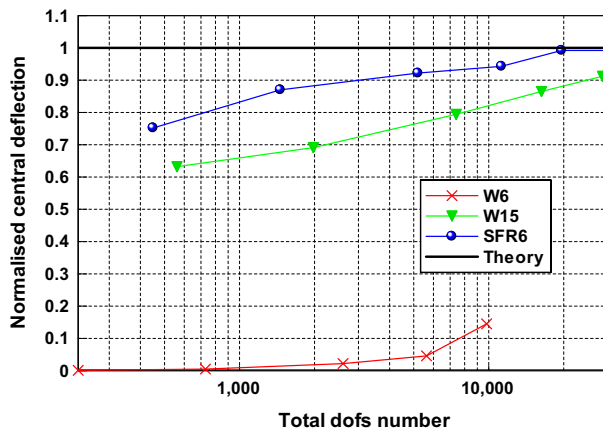
Figure 13. Normalised central deflection for 30° skew plate (*R/h* = 1000).

the thick plate case (*L/h* = 100), the performance of the present element is comparable with that of the W15 element.

4.6. Twisted beam

The clamped thick twisted beam shown in Figure 14, under in-plane and out-of-plane unit loading at its free end, is analysed. This problem was proposed by MacNeal and Harder (1985). Originally, this test was introduced to investigate the performance of finite elements in case of warped structures. The geometric and material data are specified in Table 10. The beam is gradually twisted, so that its free end is rotated by 90° in accordance to its clamped end. This problem constitutes a good test for membrane locking (Belytschko, Wong, & Stolarski, 1989). To test whether the element exhibits membrane locking, two thickness *h*'s are considered. The normalised results are summarised in Table 11. In this example, the present element is also compared to the assumed strain element SHB6 developed by Trinh, Abed-Meraim, and Combescure (2011). These results are in agreement with those obtained by SHB6 element. It is clear that superior accuracy of the SFR6 elements over the standard 6-node element is observed. Although the twisted beam is very thin (for *h* = .0032), the results of the SFR6 element are not corrupted by the membrane locking compared with W6 element. It is observed that only the W6 element exhibits membrane locking.
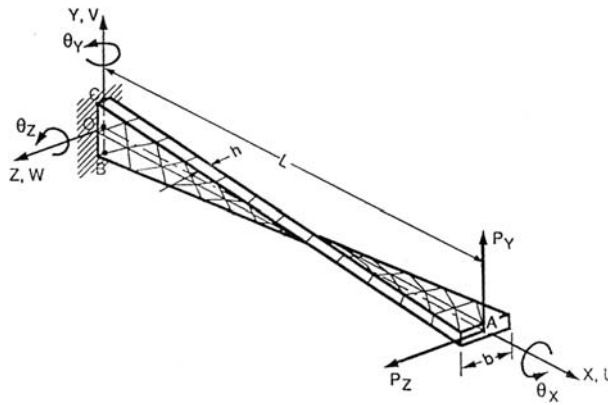
Figure 14.   Twisted beam modelled by $(12 \times 2 \times 1) \times 2$ elements.

Table 10.   Geometric and material properties of the twisted beam problem.

Length; width; and thickness	$L = 12$; $b = 1.1$; $h = .32$ and .0032
Young's modulus; Poisson's ratio	$E = 29 \times 10^6$; $v = .22$
Applied load	$p = 1.0$

Table 11.   Normalised displacement at point A of the twisted cantilever beam problem.

Elements	Mesh: (elem. along the length × elem. along the width × thick. elem.) × 2			Reference
	$12 \times 2 \times 1$	$24 \times 4 \times 1$	$36 \times 6 \times 1$	
In-plane loadings: $P_Z = 1.0$, $P_Y = 0$				
$h = .32$				
W6	.47	.73	.83	$W_A = .005424$
W15	.99	.99	.99	
SHB6	.78[a]	.93	.97[b]	
SFR6	.86	.91	.93	
$h = .0032$				
W6	.000	.001	.002	$W_A = 5316$
SFR6	.65	.73	.89	
Out-of-plane loadings: $P_Y = 1.0$, $P_Z = 0$, $h = .32$				
W6	.45	.73	.83	$V_A = .001754$
W15	.99	1.00	1.00	
SFR6	.91	.94	.96	

[a]Mesh $= (12 \times 4 \times 1) \times 2$
[b]Mesh $= (36 \times 8 \times 1) \times 2$.

4.7.   *Pinched hemisphere*

The pinched hemispherical shell with an 18° circular cutout at its pole is under alternating radial point forces at 90° intervals, proposed by MacNeal and Harder (1985), is further used to evaluate the performance of the proposed element in doubly curved structures. According to symmetry boundary conditions, only one quarter of the shell is modelled by uniform meshes as illustrated in Figure 15. The shell's dimensions are: radius $R = 10.0$ m and thickness
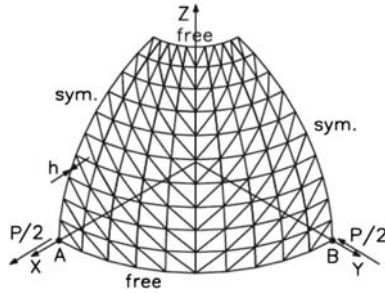
Figure 15. A quarter of the hemispherical shell with an 18° circular cutout at its pole.

Table 12. Results of the hemispherical shell with 18° hole.

Elements	Mesh: $(N \times N \times$ thick. elem.$) \times 2$					Ref.
	$2 \times 2 \times 1$	$4 \times 4 \times 1$	$6 \times 6 \times 1$	$12 \times 12 \times 1$	$24 \times 24 \times 1$	
W6	.00003	.00005	.0001	.0003	.0014	.093
W15	.0009	.0049	.0167	.0681	.0908	
SFR6	.0426	.0482	.0655	.0820	.0910	

$h = .04$ m. The material properties are: Young's modulus is $E = 6.825 \times 10^7 \, Pa$ and the Poisson's ratio is $v = .3$. The reference solution is $U_A = -V_B = .094$ m when $p = 1.0$ N, which was obtained by MacNeal and Harder (1985). Simo, Fox, and Rifai (1989) found, however, that the analytical solution of this problem yields a value of .093 m, which is used as a reference solution. Regular meshes with $N = 2, 4, 6, 12$ and 24 elements on each side of the hemisphere have been considered. The predicted radial displacements at the points of loading are compared with the converged solution of W6 and W15 elements. The comparisons between the calculated displacements are given in Table 12 and plotted in Figure 16. We also remark that SFR6 results are better than those of all the non-rotational elements (W6 and W15) and it converges quickly to the reference solution.
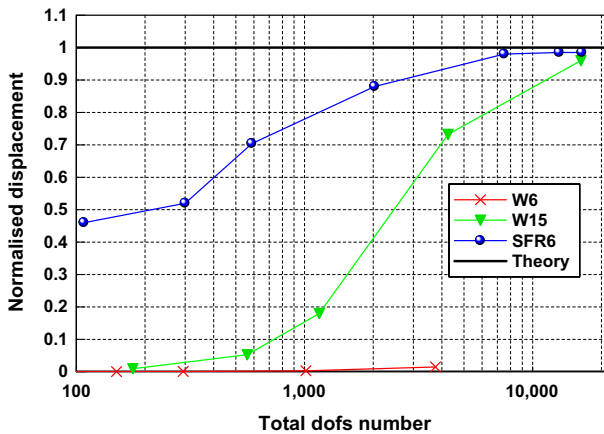

Figure 16. Pinched hemispherical shell. Convergence of the normalised displacement under the load with respect to the total DOF number (log scale).

4.8. *Pinched cylindrical shell*

Figure 17 shows a pinched cylinder subjected to a pair of concentrated loads. The cylinder is covered with rigid diaphragms so that only the displacement in the axial direction is allowed at the ends. Taking the advantage of the symmetry, only one octant of the cylinder is modelled and an $N = 2, 4, 8, 12, 14$ and 24 regular mesh is employed. The analytical solution of the problem given by Lindberg et al. (1969) is: -1.82488×10^{-7} m. The computed displacements at the loading point are compared to the analytic solution given in Table 13. And the convergence test of this element is also plotted in Figure 18. Obviously, the present element appeared to be the best performers compared to the W6 and SHB6 elements. For $N = 2$ and 4, the SFR6 element results are better than those of W15 element. Besides is of comparable precision to W15 element for $N = 8, 12, 14$ and 24. SFR6 element works well in this problem, indicating that this element can avoid not only shear locking but also membrane locking; this is not unexpected since membrane locking occurs primarily in curved elements (see, e.g. Stolarski & Belytschko, 1983).

4.9. *Clamped beam*

This example was proposed by Areias et al. (2003). As shown in Figure 19, there is a clamped beam with Young's modulus $E = 1500$ and Poisson ratio $v = .25$. The clamped beam of dimension $2 \times 10 \times 2$ is modelled by three meshes with 4, 8 and 12 wedge elements. The effect of the sensitivity to mesh orientation of the SFR6 solid element on the accuracy of results can be conveniently addressed by studying the two mesh types (see Figure 19) of clamped beams. It is also a cantilever beam under pure bending (case A) or transverse bending (case B) loads. The results in the beam and the effect of the sensitivity to mesh orientations on the accuracy of results are investigated in detail. The normalised
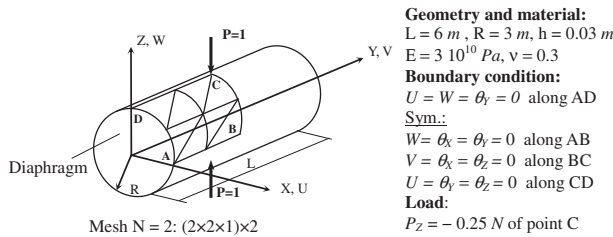

Geometry and material:
$L = 6$ m , $R = 3$ m, $h = 0.03$ m
$E = 3 \, 10^{10}$ Pa, $v = 0.3$
Boundary condition:
$U = W = \theta_Y = 0$ along AD
Sym.:
$W = \theta_X = \theta_Y = 0$ along AB
$V = \theta_X = \theta_Z = 0$ along BC
$U = \theta_Y = \theta_Z = 0$ along CD
Load:
$P_Z = -0.25$ N of point C

Mesh N = 2: (2×2×1)×2

Figure 17.   Pinched cylindrical shell.

Table 13.   Displacement for the pinched cylinder with diaphragms.

	Mesh: $(N \times N \times$ thick. elem.$) \times 2$						
Elements	$2 \times 2 \times 1$	$4 \times 4 \times 1$	$8 \times 8 \times 1$	$12 \times 12 \times 1$	$14 \times 14 \times 1$	$24 \times 24 \times 1$	Ref.
$W_{ref} = -W_C \, Eh/P$							
W6	2.434	5.553	12.401	21.116	24.177	64.081	
W15	15.46	43.22	107.01	137.74	145.47	154.05	
SHB6	–	–	39.417[a]	–	107.82[b]	–	164.24
SFR6	23.16	66.90	106.59	121.83	127.35	150.75	

[a]Mesh $(10 \times 10 \times 1) \times 2$.
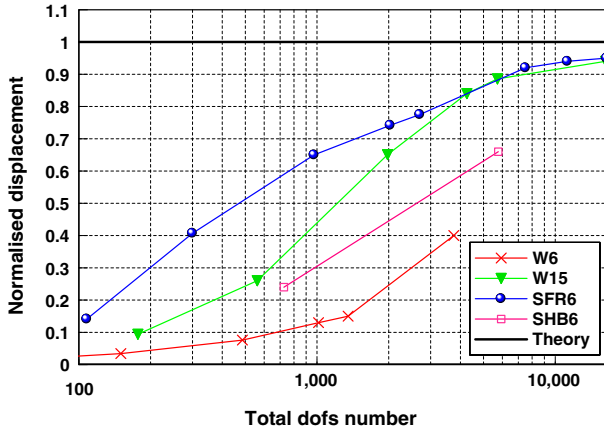[b]Mesh $(30 \times 30 \times 1) \times 2$.

Figure 18. Pinched cylinder with end diaphragms. Convergence of the normalised displacement under the load with respect to the total DOF number (log scale).
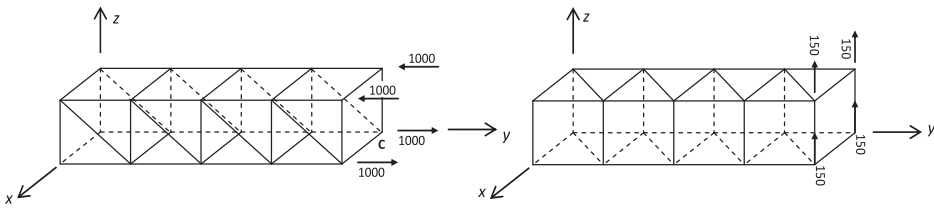

Figure 19. Clamped beams, 3D meshes with eight SFR6 elements. Left, mesh type (1), load case (A). Right, mesh type (2), load case (B).

results of deflection at point *C* are listed in Table 14. It can be seen that for the mesh type (2), the proposed solid element SFR6 produced acceptable answers. As to the mesh type (1), the accuracy obtained is not as good as that in mesh type (2). Obviously, the proposed SFR6 element is the more accurate compared to the classical six node wedge element for the two mesh types. From the observation of the table, it is possible to conclude that the SFR model is less sensitive to mesh orientation than 6-node wedge element with

Table 14. The normalised results of deflection at point *C* for clamped beam tests.

	Elements					
	W6		W15		SFR6	
Mesh	Type 1	Type 2	Type 1	Type 2	Type 1	Type 2
Load case (A): normalised deflections at point C, exact solution: 100						
$(1 \times 2 \times 1) \times 2$	.09	.64	.96	.97	.58	.89
$(1 \times 4 \times 1) \times 2$	.19	.86	.98	.98	.69	.92
$(1 \times 6 \times 1) \times 2$	.24	.90	.99	.99	.86	.95
Load case (B): normalised displacements at point C, exact solution: 102.6						
$(1 \times 2 \times 1) \times 2$	.11	.59	.93	.95	.56	.80
$(1 \times 4 \times 1) \times 2$	.21	.83	.97	.97	.69	.90
$(1 \times 6 \times 1) \times 2$	.25	.88	.98	.98	.88	.96

translations only as DOF, much better than W6 element for mesh type (1). From this example, we see that even for the mesh type (1), the W15 element gives very accurate results when compared with the exact solution.

4.10. *Simply supported square plate problem*

The purpose of this test is to see if shear locking occurs as the thickness of a square plate is reduced in comparison to its lateral dimensions. A square plate with a simply supported boundary condition at all edges is considered. This problem is illustrated in Figure 20. The plate is subjected to uniformly distributed load $q = 1$. Owing to symmetry, one quarter of the plate is considered and discretised with $(6 \times 6 \times 1) \times 2$ SFR6 elements. Central deflections are normalised with Kirchhoff plate theory solution (see Timoshenko & Woinowsky-Krieger, 1961). The normalised results of the central deflection are shown in Table 15. And the convergence tests of the normalised transverse displacement in terms of the length to thickness ratio are also plotted in Figure 21. It can be recognised that W6 element still shows considerable shear locking, whereas the SFR model renders sufficient results even for an extremely thin plate. Though SFR6 element does not suffer from shear locking, its accuracy is inferior to that of W15. Nevertheless, SFR6 seems to suffer from the Poisson's thickness locking due to the use of more than one element across the thickness. Therefore, more than one element (two elements here) should be used across the thickness in order to obtain a good result in bending dominated problems.
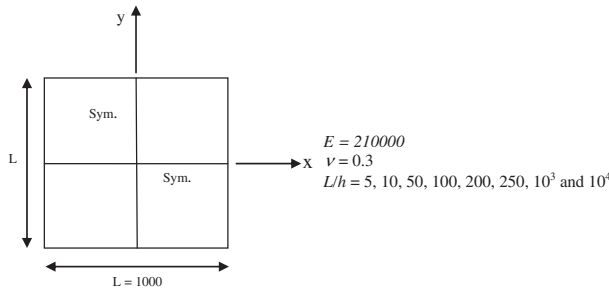

Figure 20.   Simply supported square plate with uniform loading – plan view.

Table 15.   Normalised central deflection for simply supported square plate under a distributed load.

L/h	SFR6	SFR6 2 th. el.	W6	W6 2 th. el.	W15
5	1.08	1.23	1.01	1.11	1.32
10	.91	1.05	.75	.84	1.11
50	.84	.98	.19	.21	1.01
100	.83	.97	.07	.07	1.00
200	.83	.97	.02	.02	.99
250	.83	.97	.01	.01	.99
10^3	.82	.96	.00	.00	.99
10^4	.80	.91	.00	.00	.98

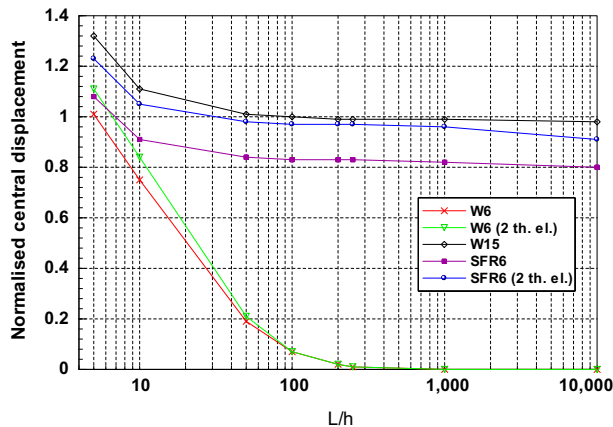Note: th. el., elements across the thickness.

Figure 21. Simply supported square plate with uniform loading: convergence of the normalised central displacement in terms of the length to thickness ratio (log scale).

5. Summary and conclusions

In this paper, a new 6-node solid wedge element called SFR6 with six degrees of freedom (three translations and three fictive rotations) per node based upon the SFR concept is developed. To this, SFR is introduced to enrich the displacement field. After identifying all the zero-energy modes, stabilisation scheme is formulated by using the penalty stiffnesses. The new element passes the patch test and with mode control does not contain any zero-energy modes. The goal of this paper is to present a new 6-node solid wedge element with only two integration points which is significantly superior to the classical 6-node wedge element with translation only and is not computationally as expensive as a 15-node wedge element. From numerical simulations, it is found that the present element exhibits favourable behaviour in 3D structures. Additionally, the present formulation is less sensitive to mesh distortion compared with the linear 6-node wedge element and is free of shear locking and membrane locking. Overall, the present element has proven its capability to solve different structural problems successfully and efficiently. The results presented in this paper are concerned with linear elasticity at small strains support this effort.

References

Allman, D.J. (1984). A compatible triangular element including vertex rotations for plane elasticity analysis. *Computers & Structures, 19*, 1–8.

Allman, D.J. (1988). Evaluation of the constant strain triangle with drilling rotations. *International Journal for Numerical Methods in Engineering, 26*, 2634–2655.

Areias, P.M.A., Cesar, S.J.M.A., Antonio, C.A.C., & Fernandes, A.A. (2003). Analysis of 3D problems using a new enhanced strain hexahedral element. *International Journal for Numerical Methods in Engineering, 58*, 1637–1682.

Ayad, R. (1993). *Mixed plate and shell finite elements with shear projection* (Phd thesis, University of Technology of Compiègne, France).

Ayad, R. (2003). A 3D 8-node solid element based upon the space fiber rotation concept (In French). *Proceedings of the 16th French Congress on Mechanics*, Nice, France.

Babuska, I., & Scapolla, T. (1989). Benchmark computation and performance evaluation for a rhombic plate bending problem. *International Journal for Numerical Methods in Engineering, 28*, 155–179.

Batoz, J.L., & Dhatt, G. (1990). Modeling of structures by finite elements. Vol. 1 - Elastic solids. Paris: Hermès.

Batoz, J.L., & Dhatt, G. (1992). Modeling of structures by finite elements. Vol. 3 - Shells. Paris: Hermès.

Belytschko, T., Wong, B.K., & Stolarski, H. (1989). Assumed strain stabilization procedure for the 9-node Lagrange shell element. *International Journal for Numerical Methods in Engineering, 28*, 385–414.

Bergan, P.G., & Felippa, C.A. (1984). A triangular membrane element with rotational degrees of freedom. *Computer Methods in Applied Mechanics and Engineering, 50*, 25–69.

Cook, R.D. (1986). On the Allman triangle and a related quadrilateral element. *Computers & Structures, 22*, 1065–1067.

Cook, R.D. (1987). A plane hybrid element with rotational DOF and adjustable stiffness. *International Journal for Numerical Methods in Engineering, 24*, 1499–1508.

Cook, R.D., Malkus, D.S., & Plesha, M.E. (1989). *Concepts and applications of finite element analysis* (3rd ed.). New York, NY: Wiley.

Dhondt, G. (2004). *The finite element method for three-dimensional thermomechanical applications*. Hoboken: Wiley.

Flanagan, D.P., & Belytschko, T. (1981). A uniform strain hexahedron and quadrilateral with orthogonal hourglass control. *International Journal for Numerical Methods in Engineering, 17*, 679–706.

Ghomari, T., Talbi, N., Ayad, R., Kerdal, D.E., & Ziane, M. (2006). An axisymmetric hyperelastic solid model for forming processes of hollow plastic bodies. *Journal of Applied Sciences, 6*, 1251–1257.

Lindberg, G.M., Olson, M.D., & Cowper, G.R. (1969). New developments in the finite element analysis of shells. *Qarterly Bulletin of the Division of Mechanical Engineering National Aeronautical Establishment, 4*, 1–99.

MacNeal, R.H. (1989). Toward a defect-free four-noded membrane element. *Finite Elements in Analysis and Design, 5*, 31–37.

MacNeal, R.H., & Harder, R.L. (1985). A proposed standard set of problems to test Finite element accuracy. *Finite Elements in Analysis and Design, 1*, 1–20.

MacNeal, R.H., & Harder, R.L. (1988). A refined four-noded membrane element with rotational degrees of freedom. *Computers & Structures, 28*, 75–84.

Mahnken, R., Caylak, I., & Laschet, G. (2008). Two mixed finite element formulations with area bubble functions for tetrahedral elements. *Computer Methods in Applied Mechanics and Engineering, 197*, 1147–1165.

Matsubara, H., Iraha, S., Tomiyama, J., Yamashiro, T., & Yagawa, G. (2004). Free mesh method using a tetrahedral element including vertex rotations. *JSCE Journal of Structural Mechanics and Earthquake Engineering, 766*, 97–107.

Morley, L.S.D. (1963). *Skew plates and structures*. New York, NY: MacMillan.

Pawlak, T.P., Yunus, S.M., & Cook, R.D. (1991). Solid elements with rotational degrees of freedom: Part II − tetrahedron elements. *International Journal for Numerical Methods in Engineering, 31*, 593–610.

Simo, J.C., Fox, D.D., & Rifai, M.S. (1989). On a stress resultant geometrically exact shell model. Part II: The linear theory; computational aspects. *Computer Methods in Applied Mechanics and Engineering, 73*, 53–92.

Stolarski, H., & Belytschko, T. (1983). Shear and membrane locking in curved C^0 elements. *Computer Methods in Applied Mechanics and Engineering, 41*, 279–296.

Sze, K.Y., & Pan, Y.S. (2000). Hybrid stress tetrahedral elements with Allman's rotational D.O.F.s. *International Journal for Numerical Methods in Engineering, 48*, 1055–1070.

Sze, K.Y., Soh, A.K., & Sim, Y.S. (1996). Solid elements with rotational d.o.f.s by explicit hybrid stabilization. *International Journal for Numerical Methods in Engineering, 39*, 2987–3005.

Taylor, R.L., Simo, J.C., Zienkiewicz, O.C., & Chan, A.C. (1986). The patch test: A condition for assessing finite element convergence. *International Journal for Numerical Methods in Engineering, 22*, 39–62.

Tian, R., Matsubara, H., & Yagawa, G. (2006). Advanced 4-node tetrahedrons. *International Journal for Numerical Methods in Engineering, 68*, 1209–1231.

Timoshenko, S.P., & Woinowsky-Krieger, S. (1961). *Theory of plates and shells*. New York, NY: McGraw-Hill.

Trinh, V.D., Abed-Meraim, F., & Combescure, A. (2011). A new assumed strain solid–shell formulation "SHB6" for the six-node prismatic finite element. *Journal of Mechanical Science and Technology, 25*, 2345–2364.

Yunus, S.M. (1988). A study of different hybrid elements with and without rotational DOF for plane stress/plane strain problems. *Computers & Structures, 30*, 1127–1130.

Yunus, S.M., Pawlak, T.P., & Cook, R.D. (1991). Solid elements with rotational degrees of freedom: Part I – hexahedron elements. *International Journal for Numerical Methods in Engineering, 31*, 573–592.

Yunus, S.M., Saigal, S., & Cook, R.D. (1989). On improved hybrid finite elements with rotational degrees of freedom. *International Journal for Numerical Methods in Engineering, 28*, 785–800.

Yuqiu, L., & Yin, X. (1994). Generalized conforming triangular membrane element with vertex rigid rotational freedom. *Finite Elements in Analysis and Design, 17*, 259–271.

Zienkiewicz, O.C. (1977). *The finite element method*. London: McGraw-Hill.